

¹ The imbricated foreshock and aftershock activities of
² the Balsorano (Italy) M_w 4.4 normal fault earthquake
³ and implications for earthquake initiation

⁴ H. S. Sánchez-Reyes¹, D. Essing¹, E. Beaucé², P. Poli¹¹

⁵ *¹Institute of Earth Sciences, University Grenoble Alpes, Grenoble 38100, France*

⁶ *²Department of Earth, Atmospheric, and Planetary Sciences, Massachusetts Institute of
7 Technology, Cambridge, MA, United States*

⁸ **Corresponding author: hugo.sanchez-reyes@univ-grenoble-alpes.fr*

⁹ **Key words:**

¹⁰ • earthquake initiation process

¹¹ • earthquake sequence

¹² • spatio-temporal evolution

¹³ **Key points:**

¹⁴ • The analysis of the 2019 Balsorano earthquake sequence reveals that imbricated com-
¹⁵ plex processes occur before and after the main earthquake

¹⁶ • Clear differences between foreshocks and aftershocks are highlighted by the distinct
¹⁷ spatio-temporal patterns unraveled by our analysis

¹⁸ • These results demonstrate that simple earthquake preparation models are not suitable
¹⁹ enough to correctly mimic the observed complex reality

20

Abstract

21 Foreshocks in the form of microseismicity are among the most powerful tools to
22 study the physical processes that occur before main earthquakes. However, their de-
23 tection and precise characterization is still sparse, especially for relatively small to
24 moderate-sized earthquakes ($M_w < 5$). ($M_w < 6$). We present here a detailed fore-
25 shock analysis for the November 7, 2019, Balsorano (Italy) normal fault earthquake
26 ($M_w 4.4$). To improve the detection of the microseismicity before and after the main-
27 shock, we use six three-component broadband receivers at distances of less than 75
28 km from the targeted seismicity, through template matching. To improve the under-
29 standing of the physical mechanism(s) behind the earthquake initiation process, as
30 well as other accompanying phenomena, we also detail the spatio-temporal evolution
31 of the sequence associated to this medium-sized earthquake, using waveform cluster-
32 ing and hypocenter relocation. Clear differences between foreshocks and aftershocks
33 are revealed by this analysis. Moreover, five distinct spatio-temporal patterns asso-
34 ciated to the different seismic activities are revealed. The observed spatio-temporal
35 behavior shown by the foreshocks highlights a complex initiation process, which ap-
36 parently starts on an adjacent unmapped antithetic fault. Finally, the aftershock ac-
37 tivity comprises four different clusters with distinct spatio-temporal patterns, which
38 suggests that each cluster the different clusters in this sequence has a have distinct
39 triggering mechanism. mechanisms.

40

Introduction

41 The detection of signals that can inform us about an incoming a forthcoming earthquake
42 is fundamental to build physical models that mimic the processes behind the triggering
43 and nucleation of earthquakes. These physical models are important because they pro-
44 vide us the basis to characterize earthquakes. Therefore, the study and analysis of pre-
45 cursory signals are of great importance. Over the last 25 years, numerous studies have

46 reported a wide range of observations that appear to be connected with the physics that
47 precedes large seismic events (*e.g.* Rikitake, 1975; Jones and Molnar, 1979; Molchanov
48 et al., 1998; Eftaxias et al., 2000; Virk and Walia, 2001; Singh et al., 2010; De Santis
49 et al., 2019; Jones, 1985; Abercrombie and Mori, 1996; Felzer et al., 2004; Dodge et al.,
50 1996; Ellsworth and Bulut, 2018; Yoon et al., 2019; Reasenberg, 1999; Ruiz et al., 2017,
51 2014a). Among these, some of the most compelling are the more significant ones have
52 been based on seismological characterization of foreshock sequences sequences, as well
53 as other seismological observations and their relationships with mainshocks (*e.g.* Jones,
54 1985; Abercrombie and Mori, 1996; Reasenberg, 1999; Felzer et al., 2004; Dodge et al.,
55 1996) Bouchon₂₀₁₁_{ENI}, Ruiz₂₀₁₄_{IFS}, ruiz₂₀₁₇_{nucleation}, Ellsworth₂₀₁₈_{IE}; ?Yoon₂₀₁₉_{FMN}, ruiz₂₀₁₇_{IE}).
56 Foreshocks are thus one of the most useful tools to understand the physics of earthquake
57 initiation in real faults (Brune, 1979; Abercrombie and Mori, 1996; Malin et al., 2018).
58 Therefore, it is important to improve foreshock observations and characterization, even
59 particularly for the more frequent medium-sized small to moderate-sized events (*i.e.* $M_w <$
60 6), as these might share similar physical processes with larger events. These improved ob-
61 servations may shed new light on the physical processes that occur during the triggering
62 and nucleation of earthquakes and will drive future research that focuses on theoretical and
63 numerical models to better characterize earthquake occurrence in real and complex faults.

64 Earthquake initiation (*e.g.* Kato et al., 2012; Schurr et al., 2014; Tramutoli et al., 2015)
65 and earthquake nucleation/triggering (*e.g.* Dieterich, 1992; Ellsworth and Beroza, 1995;
66 Rubin and Ampuero, 2005) are two different, and perhaps overlapping, phases of the seis-
67 mic cycle. While the first is understood to occur over the longer term preceding a large
68 event (*i.e.*, days or months, to years), the second occurs some minutes to The results of
69 the spatio-temporal evolution for the identified clusters suggest complex evolution of the
70 seismicity. Two fault planes are activated during the sequence, with foreshocks primarily
71 occurring on the antithetic fault plane (Fig. 5a, cross-section), similarly to part of the
72 foreshock activity that was observed for the L'Aquila normal fault earthquake (Chiara
luce

73 et al., 2011). Relying only on our observations, it is hard to unravel which mechanism(s)
74 might be responsible for the occurrence of the foreshocks, and thus the driving of the
75 main event. For example, there are no exponential or power-law increments of events seen
76 while approaching the main event (Papazachos, 1975; Kagan and Knopoff, 1978), which
77 might suggest accelerating aseismic slip (Dodge et al., 1996; Bouchon et al., 2011; Tape
78 et al., 2018). Neither are any spatial patterns seen (*e.g.*, migrations) that might suggest
79 the same mechanism, or might alternatively indicate triggering by stress transfer (Dodge
80 et al., 1996; Ellsworth and Bulut, 2018; Yoon et al., 2019). However, we clearly outline the
81 differences between the foreshocks and aftershocks. In particular, the foreshocks occur in a
82 more temporal clustered manner, and they are closer to the hypocenter of the main event
83 (Fig. 4a). The compact and highly temporal clustered seismicity indicates strong event
84 interactions, and favors stress transfer as the mechanism for foreshock occurrence (COV,
85 Schoenball and Ellsworth, 2017). seconds before the main event. Both phases, however,
86 can be explained under the Dieterich model (1994), which relates the seismicity rate to the
87 stressing history through a rate-and-state constitutive law. For earthquake initiation in
88 particular for real faults, two main hypotheses are currently used to explain this process.
89 Some authors argue that a mainshock is a consequence of a cascade process, with stress
90 transfer in-between events, which eventually trigger the large event (*e.g.*, Dodge et al., 1996;
91 Ellsworth and Bulut, 2018; Yoon et al., 2019). Alternatively, the initiation of an earthquake
92 can be understood as an aseismic process that weakens the pre-existing asperities, until a
93 larger rupture is promoted (Dodge et al., 1996; Bouchon et al., 2011; Tape et al., 2018). In
94 the latter case, foreshocks result from the activation of brittle asperities by the surrounding
95 slip processes. However, intermediate models that involve both triggering and aseismic slip
96 are likely for complex faults (*e.g.* McLaskey, 2019). This complexity might result from fault
97 heterogeneity (*e.g.*, variable stress, frictional properties) and promote imbricated sequences
98 of foreshocks and aseismic slip (*e.g.*, Dublanchet, 2018).

99 The monitoring of foreshocks is today routine in laboratory experiments (Zang et al.,

100 1998; Goebel et al., 2012; Renard et al., 2019, and references therein), while studies that
101 focus on large earthquakes remain relatively sparse (*i.e.*, $M_w > 6$) (*e.g.*, Mogi, 1963; Aber-
102 crombie and Mori, 1996; Kato et al., 2012; Chen and Shearer, 2013; Bouchon et al.,
103 Ruiz2014IFS, ruiz2014intense.Ruiz2014IFS; ?). However, the recent improvements
104 to seismological monitoring systems around active faults have now provided detailed anal-
105 ysis of foreshocks that precede the more frequent small-magnitude small to moderate-sized
106 earthquakes ($M_w < 6$) (*e.g.*, Savage et al., 2017; McMahon et al., 2017; Malin et al., 2018).
107 One intriguing feature that has emerged from these last more recent studies is the in-
108 creased complexity (*i.e.*, fault interactions, volumetric processes) that have been revealed
109 through the availability of better data (*e.g.*, near-fault receivers) and more advanced de-
110 tection methods (*e.g.*, template matching) to study foreshocks. This complexity might
111 challenge the actual laboratory scale and theoretical models, which treat earthquake ini-
112 tiation as simple physical processes that occur in smooth fault planes (Dieterich, 1992;
113 Marone, 1998; Rubin and Ampuero, 2005; Liu and Rice, 2005). The necessity for high-
114 resolution characterization of foreshocks based on good data and advanced data processing
115 techniques was also suggested by a meta-analysis carried out by Mignan (2014), which in-
116 dicated resolution-dependent bias for earthquake initiation models that were resolved using
117 seismological data.

118 To shed new light on the physical processes that occur before relatively small earth-
119 quakes, we study here the medium-sized ($M_w 4.4$) Balsorano normal fault earthquake and
120 its foreshock-aftershock sequence (Fig. 1). The Italian National Institute of Geophysics and
121 Volcanology (*Istituto Nazionale di Geofisica e Vulcanologia*; INGV; [online catalog](#)) reported
122 that the main event of this sequence occurred on November 7, 2019 (17:35:21.18 UTC), ap-
123 proximately 4 km southeast of Balsorano city in central Italy (Fig. 1). The hypocenter of
124 this main event was located relatively deep in the crust (~ 15 (14 km), close to the transi-
125 tion zone between the upper and lower crust (10-20 km in depth), where the brittle locked
126 fault transitions into the ductile regime zone (Doglioni et al., 2011). Below this depth, the

127 lower crust is relatively seismically silent (Doglioni et al., 2011). According to a geological
128 study of the location of the main event and its focal mechanism (Supplementary Material
129 Table S1), this event ruptured the Liri fault (Roberts and Michetti, 2004), which is one of
130 the major active normal faults mapped in this region. This structure accommodates the
131 low extension rate observed in this region (*i.e.*, a few millimeters per year) (Hunstad and
132 England, 1999; Westaway, 1992; D'agostino et al., 2001; Roberts and Michetti, 2004).

133 [Figure 1]

134 In addition to the mainshock of November 7, 2019, 135 events occurred close to the
135 epicenter of the main event from October 22 to November 15, 2019 (which included 25
136 foreshocks). Starting from these cataloged events, we study here the 'anatomy' of the
137 foreshocks and aftershocks, and their relationships with the main event. With this aim,
138 continuous data from six three-component stations at less than 75 km from the mainshock
139 epicenter are used (Fig. 1; Supplementary Materials Table S2). The continuous waveforms
140 recorded are analyzed using template matching techniques (Gibbons and Ringdal, 2006;
141 Shelly et al., 2007) to detect smaller events and thus to expand upon the available seismic
142 catalog. The detected events are then relocated using the double-difference method (Wald-
143 hauser, 2001), to reveal the geometry of the main fault and to obtain new insights into
144 the fault-slip behavior(s) before and after the main seismic event. Furthermore, through
145 waveform clustering, we isolate families of earthquakes that are representative of different
146 physical processes that occur in the pre- and post-mainshock period. This combination of
147 detection, relocation, and waveform clustering reveals an imbricated seismic sequence where
148 several faults were activated, and with clear differences in the spatio-temporal properties
149 of the foreshocks and aftershocks.

150 Methods

151 **Template matching:** The analysis starts by extending the INGV seismic catalog using the

template matching approach (Gibbons and Ringdal, 2006). From the 135 events reported by the INGV online catalog , where 25 events are identified as foreshocks, we retain only the events with available P-wave and S-wave picks for all of the six stations used. We then extract 4 s of signal, starting 1 s before the phase arrival time from the band-pass filtered data (5-20 Hz). Using the pre-picked signals, we estimate the signal-to-noise ratio and retain as templates only those events with a signal-to-noise ratio >3 at all of the stations. With this data selection, 23 events are obtained (including three foreshocks) that are the templates used for scanning the continuous data (Supplementary Materials Table S4). We use three-component data with P waves extracted from the vertical component, and S waves extracted from the East and North components.

In all, 28 days of continuous data are processed, from October 22 (*i.e.*, 16 days before the mainshock) to November 15, 2019, using the fast matched filter algorithm from Beaucé et al. (2017). The detection thresholds are set to 12 times the daily median absolute deviation of the summed correlation coefficients over the array of stations. Finally, consecutive detections with differential times of <3 s are removed (*i.e.*, the time difference between two estimated origin times).

The final catalog contains 714 events (166 foreshocks, 547 aftershocks), which represents ~ 6 -fold the number of events in the initial catalog. To estimate the magnitudes of the newly detected events, we use the average root mean square in the time window containing the S waves over all of the stations and components. Least-square fitting is then used to obtain a linear model that relates the logarithmic of the root mean square of the 23 templates and their local magnitudes from the INGV catalog. This model is then used to estimate the magnitude of the newly detected events. A summary of the event occurrences in time together with their magnitudes is shown in Figure 2.

176

[Figure 2]

177 **Waveform-based clustering:** Clustering is widely used in seismology to recognize

178 patterns in spatio-temporal events, which include the identification of foreshock-aftershock
179 sequences and stress evolution in time (*e.g.*, Kagan and Jackson, 1991; Wehling-Benatelli
180 et al., 2013; Cesca et al., 2014; Ellsworth and Bulut, 2018). Here, we apply waveform simi-
181 larity analysis (Cattaneo et al., 1999) to define groups of events that share similar locations
182 and/or a common rupture mechanism (Kagan and Jackson, 1991; Wehling-Benatelli et al.,
183 2013; Cesca et al., 2014; Ellsworth and Bulut, 2018; Cattaneo et al., 1999). For this, the
184 full normalized waveforms are used, with a 4.5-s time window (starting 0.5 s before the
185 P-wave arrival) that contains both the P phase and the S phase.

186 The waveforms of the 714 detected events recorded at the closest station to the epicenter
187 (Fig. 1, VVLD) are then correlated with each other. The correlation matrix obtained (Fig.
188 3a) is used to estimate the distance (dissimilarity) metric to perform hierarchical clustering.
189 The Ward minimum variance method is used (Ward Jr, 1963) with a distance threshold
190 of 5.5 defined (Supplementary Materials Fig. S1: the largest separation observed from
191 the dendrogram). This waveform similarity analysis highlights five different clusters, as
192 shown in Figure 3b, c. As both the P waves and S waves are used for clustering, the
193 resulting family members should share share, to some extend, similarities in position and
194 rupture mechanism (Kagan and Jackson, 1991; Wehling-Benatelli et al., 2013; Cesca et al.,
195 2014; Ellsworth and Bulut, 2018; Cattaneo et al., 1999). However, due to the proximity
196 to the study region of the recording station used in this analysis (VVLD), short S-P time
197 differences are observed for most of the events in the sequence. Therefore, it is important
198 to keep in mind that events occurring in different locations with similar mechanisms might
199 appear strongly related.

200 **Relocation:** We finally estimate the relative location between the detected events using
201 the double-difference algorithm (HypoDD software; Waldhauser (2001)). The differential
202 times of the P phases and S phases between events from the cross-correlation are estimated,
203 with the retention of only the delays that are associated to correlation coefficients >0.6 .
204 We further limit the delays to 0.2 s. After discarding the event pairs that relate less than

205 3 P-wave and 3 S-wave highly correlated differential times (correlation coefficient, ≥ 0.6),
206 the final number of 29859 pairs are kept and used in the relocation process.

207 For each newly detected event, we assume its initial location as the coordinates of the
208 template that reports the highest correlation coefficient related to that event. In addition,
209 we assume the estimated P-wave and S-wave picks obtained from our template matching
210 analysis as the initial catalog information for the relocation. A velocity model for this region
211 proposed by Bagh et al. (2007) is used in the relocation process (Supplementary Materials
212 Table S3). Following previous studies (Shelly and Hardebeck, 2019), the inversion is per-
213 formed with stronger weights to the initial information related to the P-wave and S-wave
214 picks from the catalog (*i.e.*, from the template matching analysis), while the differential
215 times from the waveform correlations control the final iterations. In the end, 689 of the
216 714 newly detected events are successfully relocated. The temporal and geometric patterns
217 observed in this earthquake sequence are illustrated in Figures 4 and 5, and are further
218 described in the following section.

219 [Figure 3]

220 Results and discussion

221 The time evolution of the detected events is shown in Figure 2. Of the 714 events, 166 are
222 foreshocks (23%). Together with the temporal evolution, Figure 2a shows the spectrogram
223 and the average spectral energy in a frequency band from 5 Hz to 20 Hz. The oscillation of
224 this energy suggests variable noise levels in the study area, with lower noise during the night
225 (Figure 2, shaded areas, for periods from 18:00 to 06:00). This noise variation is related to
226 anthropogenic activity (?), and it is also observed for the other five receivers. This noise
227 evolution will probably affect our detection performance. For example, it is not clear if
228 the reduced number of events observed prior to the mainshock is real or is a consequence

229 of the higher noise level (Fig. 2b). We thus avoid discussing any issue related to pre-
230 seismic quiescence here. However, with the geometric and clustering information derived
231 above, we can still characterize some of the properties of the newly detected foreshocks and
232 aftershocks, and gain insight into the physical processes that occur at the different stages
233 of the sequence.

234 The results from the combination of waveform clustering and relocation strategies are
235 summarized in Figures 4 and 5. For each cluster, the coefficient of variation (COV) is also
236 estimated from the recurrence time of the events (Kagan and Jackson, 1991; Schoenball
237 and Ellsworth, 2017). The COV indicates the level of the temporal clustering within each
238 group (*i.e.*, how much the occurrence of future earthquakes depends on the occurrence of the
239 past earthquakes): with COV=1 for random seismicity, and COV>1 for strong temporal
240 clustering. The larger the COV, the more the earthquakes are interacting. Thus, it is
241 important to note that events that happen together with a high COV mean that there is
242 an intrinsically related interaction between them.

243 The temporal and spatial densities of the different clusters identified in this sequence
244 are illustrated in Figure 4, where cluster 1 (green solid lines and dots) is mainly composed
245 of foreshocks (161 of 209 events occurred before the mainshock). The events that form this
246 family show the highest waveform similarity (Fig. 3a). In agreement with this waveform
247 property, cluster 1 has high spatial density, with approximately 90% of its activity (193
248 of the 208 events) located within 0.5 km of the mainshock hypocenter (Figs. 4a and 5a).
249 Cluster 1 also shows the highest temporal clustering (COV=4.8; Fig. 4a).

250 The next two families, as cluster 2 (COV=3.0; Figure 4b, blue solid lines and dots)
251 and cluster 3 (COV=2.9; Figure 4c, magenta solid lines and dots), share similar temporal
252 clustering values, but show differences with respect to their spatial densities. While ap-
253 proximately 90% of the events of cluster 2 are within 0.8 km of the hypocenter (136 of 151
254 events; Fig. 4b), cluster 3 has almost 90% of its activity (187 of 211 events) located over
255 a larger volume, as approximately 1.2 km from the mainshock location (Fig. 4c). Cluster

256 4 (Figure 4d, brown solid lines and dots) is characterized by 90% of its activity within 0.6
257 km of the mainshock hypocenter (53 of 59 shocks; Fig. 4d). The seismicity in this cluster
258 is also characterized by high temporal clustering ($\text{COV}=4.2$). Cluster 5 ($\text{COV}=2.2$; Figure
259 4e, red solid lines and dots) is the least temporally clustered, but with the second highest
260 spatial density (after cluster 1), with 90% of its activity in a region 0.5 km from the main-
261 shock hypocenter (66 of 73 events; Fig. 4e). A general spatial pattern of this sequence is
262 the concentration of events close to the mainshock that occurred prior to it (110 foreshocks
263 within 0.3 km) and the subsequent spread over a region >0.3 km during the aftershocks.

264 Figure 5 illustrates the geometric patterns related to each of the clusters, as defined
265 by the relocation process. A remarkable pattern can be seen in Figure 5a: cluster 1 (*i.e.*,
266 foreshocks) shows an antithetical orientation with respect to the assumed fault plane of
267 the main event (Fig. 5a, map view and cross sections). In contrast, clusters 4 and 5 show
268 nearly parallel orientations with respect to the assumed main fault plane (Fig. 5d, e, cross-
269 sections, respectively). We also observe particular behavior for cluster 5, which is the only
270 cluster where the activity is exclusively to the northeast of the mainshock hypocenter and
271 on the footwall (Fig. 5e, map view and cross-sections). The events in cluster 5 follow an
272 orientation that is parallel to the assumed main fault plane dipping angle (Fig. 5e, cross-
273 section). In turn, cluster 3 has an activity that follows the orientation of the fault plane, but
274 that spreads across the whole volume surrounding the fault plane (Fig. 5c, cross-sections).

275 [Figure 4]

276 [Figure 5]

277 The results of the spatio-temporal evolution for the identified clusters suggest complex
278 evolution of the seismicity. Two fault planes are activated during the sequence, with fore-
279 shocks primarily occurring on the antithetic fault plane (Fig. 5a, cross-section), similarly to
280 part of the foreshock activity that was observed for the L'Aquila normal fault earthquake

281 (Chiaraluce et al., 2011). Relying only on our observations, it is hard to unravel which
282 mechanism(s) might be responsible for the occurrence of the foreshocks, and thus the driv-
283 ing of the main event. For example, there are no exponential or power-law increments
284 of events seen while approaching the main event (Papazachos, 1975; Kagan and Knopoff,
285 1978), which might suggest accelerating aseismic slip (Dodge et al., 1996; Bouchon et al.,
286 2011; Tape et al., 2018). Neither are any spatial patterns seen (*e.g.*, migrations) that might
287 suggest the same mechanism, or might alternatively indicate triggering by stress transfer
288 (Dodge et al., 1996; Ellsworth and Bulut, 2018; Yoon et al., 2019). However, we clearly
289 outline the differences between the foreshocks and aftershocks. In particular, the fore-
290 shocks occur in a more temporal clustered manner, and they are closer to the hypocenter
291 of the main event (Fig. 4a). The compact and highly temporal clustered seismicity indi-
292 cates strong event interactions, and favors stress transfer as the mechanism for foreshock
293 occurrence (COV, Schoenball and Ellsworth, 2017).

294 Analyzing the waveform-based correlation matrix (figure 3a), which is built based only
295 on the similarity of waveforms on the vertical component at the closest station, we are
296 able to distinguish approximately 60 pairs with correlation coefficients larger than 0.95.
297 However, given the fact that most of the events in the sequence have significantly small
298 magnitudes (70% of the events have magnitudes lower than 0.5, figure 2c) and that the
299 frequency range used in the analysis is limited from 5 to 20 Hz, we consider that the
300 available information does not allow us to properly conclude anything about the existance
301 of repeaters in this earthquake sequence (Uchida, 2019; Uchida and Bürgmann, 2019).

302 Interestingly, the aftershock clusters also show different spatio-temporal behaviors be-
303 tween each other (Figs. 5b-e, 4b-e). The observed differences might be explained by different
304 physical processes driving the aftershock occurrence. For example, the events in clusters
305 2 and 3 (Fig. 5b,c) spread in a volume around the fault. This spatial pattern is likely
306 to result from stress redistribution, volumetric damage, and relaxation processes after the
307 mainshock (Trugman et al., 2020). In contrast, clusters 4 and 5 follow the orientation of

308 the main fault in a more compact volume around it (Fig. 5d,e), and their activity decays
309 in a rapid manner (Fig. 4). This behavior might suggest that these latter clusters result
310 from stress increments induced by the mainshock afterslip that occurs near the fault plane
311 region in the few hours or days after the main event (Stein and Lisowski, 1983; Shen et al.,
312 1994). These particular features from clusters 4 and 5 might support the alternative model
313 proposed by ? where the afterslip from the mainshock might be the triggering mechanism
314 of the aftershocks off of the main fault.

315 It is important to point out a particular feature exhibited by cluster 3. Looking at the
316 relative small amplitude of the stacked waveform estimated for cluster 3 (figure 3c) and
317 the resulting relocation of events (figure 5c), we consider that cluster 3 is composed of all
318 the events that share a strong dissimilarity to the remaining events of the sequence. As
319 it was mentioned before, we use the dissimilarity between the waveforms recorded at the
320 closest station to the study region to infer the five different clusters. Therefore, while most
321 of the events show short S-P time differences, these events might be occurring in different
322 locations with similar mechanisms, which is exactly the case of the events from cluster 3.

323 The geometry of the subfaults that were activated during this sequence are not known
324 (except from the main Liri fault). In addition, the focal mechanisms of most of the earth-
325 quakes in the sequence can not be determined due to their small size, noise levels and
326 limited azimuthal coverage of the regional network. The slip distribution of the mainshock
327 and other subevents have not been previously studied. Therefore, the available limited
328 information does not allow to perform a proper Coulomb stress analysis of this sequence
329 (Toda et al., 2011).

330 As in previous studies (McMahon et al., 2017; Savage et al., 2017; McMahon et al., 2019),
331 we can see that this detailed analysis of seismic data reveals a complex and imbricated
332 earthquake sequence, for which the mainshock initiation is unlikely to result from only the
333 evolution of physical properties (*e.g.*, stress, friction) on the main fault plane. Indeed the
334 sequence begins through an interaction between the antithetic and main faults during the

335 foreshock-mainshock sequences, similar to that observed for other events (Chiaraluce et al.,
336 2011; McMahon et al., 2019). In normal faults, this behavior can be related to preseismic
337 processes in the dilation wedge located in the hanging wall (Doglioni et al., 2011). The
338 complexity of the sequence might also emerge from fluid involvement, which is known to
339 have a significant role in the control of seismicity and its 'style' in the central Apennines
340 (Antonioli et al., 2005; ?). The stress perturbations in the antithetic fault might have
341 modified the local pore pressures, with fluid migration into the main fault, which would
342 favor the occurrence of the main event (Doglioni et al., 2011).

343 Conclusion

344 By using a combination of high-resolution detection methods, precise relocation (*e.g.*, Gib-
345 bons and Ringdal, 2006; Waldhauser, 2001) and waveform clustering, we have unveiled
346 the complexity of the sequences associated with the 2019 (M_w 4.4) Balsorano earthquake.
347 We detect 714 events that comprise this sequence. These events are classified into five
348 different seismic clusters. The differences between these clusters are highlighted by their
349 distinct spatio-temporal properties that are unveiled by the waveform-based clustering anal-
350 ysis (Kagan and Jackson, 1991; Wehling-Benatelli et al., 2013; Cesca et al., 2014; Ellsworth
351 and Bulut, 2018), and by their relative source locations (Waldhauser, 2001).

352 Our results highlight different behaviors between foreshocks and aftershocks. For exam-
353 ple, foreshocks occur in a compact region near the mainshock hypocenter, and show high
354 temporal clustering (Fig. 4a). The lack of repeating events (*i.e.*, highly correlated events
355 with correlation coefficient >0.9), strong temporal clustering, and inter-event proximity
356 might indicate that stress transfer triggering has the main role in driving the occurrence
357 of the foreshocks (Dodge et al., 1996). Nevertheless, there are no observations that can
358 exclude aseismic slip. The foreshock activity mainly take place in an antithetic fault (Fig.
359 5a), which suggests that the initiation processes do not only occur on one fault plane, but

360 involve larger volumes (Savage et al., 2017). This precursory antithetic activation has been
361 observed in other normal fault events (Chiaraluce et al., 2011) and it can be expected in
362 some gravity-driven normal fault models (Doglioni et al., 2011).

363 Furthermore, our analysis shows diversity for the aftershocks behavior. Indeed, four
364 different clusters comprise the aftershock sequences. Two of these four are spread in a
365 volume around the main fault (Fig. 5b,c), and might result from stress redistribution after
366 the mainshock (*e.g.*, caused by volumetric damage and the relaxation processes; Trugman
367 et al. (2020)). Given the rapid temporal decay of their activity and their compactness
368 and spatial orientation, the remaining two clusters appear to be driven by rapid stress
369 increments induced by the mainshock and afterslip that occur near the fault plane in the
370 few days after the mainshock (Stein and Lisowski, 1983; Shen et al., 1994).

371 In summary, this study of foreshocks and aftershocks highlights that simple preparation
372 models with evolution of stress and friction on a single fault plane are not suited to precisely
373 explain the evolution of the seismicity we observe here for a real fault. A relatively large
374 volume appears to be involved in the earthquake initiation, over a short time scale (\sim 1 day).
375 We further highlight how the full range of aftershocks is likely to be an ensemble average
376 view of different processes, which will include afterslip, volumetric damage, and relaxation.
377 Continuing to provide detailed information about foreshocks and their relationships to the
378 mainshock and aftershocks also for relatively small events can help us to develop new and
379 more realistic models that can provide better fitting of seismological observations and shed
380 new light on the initiation of earthquakes in real faults.

381 Data and resources

382 The continuous seismic data used in this study are available at the Istituto Nazionale di Ge-
383 ofisica e Vulcanologia (INGV) seismological data center (http://cnt.rm.ingv.it/webservices_and_software/;
384 last accessed, March 2020) and were downloaded using obspyDMT ([https://github.com/kasra-](https://github.com/kasra)

385 [hosseini/obspyDMT](#), Hosseini and Sigloch (2017)). The fast matched filter (Beaucé et al.,
386 2017) used in this study can be found at https://github.com/beridel/fast_matched_filter.
387 Some plots were made using the Generic Mapping Tools version 4.5.14 (www.soest.hawaii.edu/gmt;
388 Wessel and Smith (1998)). The event clustering was performed using Scikit-learn (<https://scikit-learn.org/stable/>; Pedregosa et al. (2011))
389

390 Acknowledgments

391 This research received funding from the European Research Council (ERC) under the Euro-
392 pean Union Horizon 2020 Research and Innovation Programme (grant agreement 802777-
393 MONIAULTS). Computations were performed using the Univerty of Grenoble Alpes
394 (UGA) High-Performance Computing infrastructures CIMENT
395 (<https://ciment.univ-grenoble-alpes.fr>).

396 References

- 397 Abercrombie, R. E. and Mori, J. (1996). Occurrence patterns of foreshocks to large earth-
398 quakes in the western united states. *Nature*, 381(6580):303–307.
- 399 Antonioli, A., Piccinini, D., Chiaraluce, L., and Cocco, M. (2005). Fluid flow and seis-
400 micity pattern: Evidence from the 1997 umbria-marche (central italy) seismic sequence.
401 *Geophysical Research Letters*, 32(10).
- 402 Bagh, S., Chiaraluce, L., De Gori, P., Moretti, M., Govoni, A., Chiarabba, C., Di Bar-
403 tolomeo, P., and Romanelli, M. (2007). Background seismicity in the central apennines
404 of italy: The abruzzo region case study. *Tectonophysics*, 444(1-4):80–92.
- 405 Beaucé, E., Frank, W. B., and Romanenko, A. (2017). Fast matched filter (fmf): An

- 406 efficient seismic matched-filter search for both cpu and gpu architectures. *Seismological*
407 *Research Letters*, 89(1):165.
- 408 Bouchon, M., Durand, V., Marsan, D., Karabulut, H., and Schmittbuhl, J. (2013). The long
409 precursory phase of most large interplate earthquakes. *Nature geoscience*, 6(4):299–302.
- 410 Bouchon, M., Karabulut, H., Aktar, M., Özalaybey, S., Schmittbuhl, J., and Bouin, M.-P.
411 (2011). Extended nucleation of the 1999 mw 7.6 izmit earthquake. *science*, 331(6019):877–
412 880.
- 413 Brune, J. N. (1979). Implications of earthquake triggering and rupture propagation for
414 earthquake prediction based on premonitory phenomena. *Journal of Geophysical Re-*
415 *search: Solid Earth*, 84(B5):2195–2198.
- 416 Cattaneo, M., Augliera, P., Spallarossa, D., and Lanza, V. (1999). A waveform similarity
417 approach to investigate seismicity patterns. *Natural hazards*, 19(2-3):123–138.
- 418 Cesca, S., Sen, A. T., and Dahm, T. (2014). Seismicity monitoring by cluster analysis of
419 moment tensors. *Geophysical Journal International*, 196(3):1813–1826.
- 420 Chen, X. and Shearer, P. M. (2013). California foreshock sequences suggest aseismic trig-
421 gering process. *Geophysical Research Letters*, 40(11):2602–2607.
- 422 Chiaraluce, L., Valoroso, L., Piccinini, D., Di Stefano, R., and De Gori, P. (2011). The
423 anatomy of the 2009 l'aquila normal fault system (central italy) imaged by high resolu-
424 tion foreshock and aftershock locations. *Journal of Geophysical Research: Solid Earth*,
425 116(B12).
- 426 D'agostino, N., Giuliani, R., Mattone, M., and Bonci, L. (2001). Active crustal extension in
427 the central apennines (italy) inferred from gps measurements in the interval 1994–1999.
428 *Geophysical Research Letters*, 28(10):2121–2124.

- 429 De Santis, A., Marchetti, D., Pavón-Carrasco, F. J., Cianchini, G., Perrone, L., Abbattista,
430 C., Alfonsi, L., Amoruso, L., Campuzano, S. A., Carbone, M., et al. (2019). Precursory
431 worldwide signatures of earthquake occurrences on swarm satellite data. *Scientific reports*,
432 9(1):1–13.
- 433 Dieterich, J. (1994). A constitutive law for rate of earthquake production and its application
434 to earthquake clustering. *Journal of Geophysical Research: Solid Earth*, 99(B2):2601–
435 2618.
- 436 Dieterich, J. H. (1992). Earthquake nucleation on faults with rate-and state-dependent
437 strength. *Tectonophysics*, 211(1-4):115–134.
- 438 Dodge, D. A., Beroza, G. C., and Ellsworth, W. (1996). Detailed observations of califor-
439 nia foreshock sequences: Implications for the earthquake initiation process. *Journal of*
440 *Geophysical Research: Solid Earth*, 101(B10):22371–22392.
- 441 Doglioni, C., Barba, S., Carminati, E., and Riguzzi, F. (2011). Role of the brittle–ductile
442 transition on fault activation. *Physics of the Earth and Planetary Interiors*, 184(3-4):160–
443 171.
- 444 Dublanchet, P. (2018). The dynamics of earthquake precursors controlled by effective fric-
445 tion. *Geophysical Journal International*, 212(2):853–871.
- 446 Eftaxias, K., Kopanas, J., Bogris, N., KAPIRIS, P., ANTONOPOULOS, G., and VAROT-
447 SOS, P. (2000). Detection of electromagnetic earthquake precursory signals in greece.
448 *Proceedings of the Japan Academy, Series B*, 76(4):45–50.
- 449 Ellsworth, W. L. and Beroza, G. C. (1995). Seismic evidence for an earthquake nucleation
450 phase. *Science*, 268(5212):851–855.
- 451 Ellsworth, W. L. and Bulut, F. (2018). Nucleation of the 1999 izmit earthquake by a
452 triggered cascade of foreshocks. *Nature Geoscience*, 11(7):531–535.

- 453 Falcucci, E., Gori, S., Galadini, F., Fubelli, G., Moro, M., and Saroli, M. (2016). Active
454 faults in the epicentral and mesoseismal ml 6.0 24, 2016 amatrice earthquake region,
455 central italy. methodological and seismotectonic issues. *Annals of geophysics*, 59.
- 456 Felzer, K. R., Abercrombie, R. E., and Ekstrom, G. (2004). A common origin for af-
457 tershocks, foreshocks, and multiplets. *Bulletin of the Seismological Society of America*,
458 94(1):88–98.
- 459 Gibbons, S. J. and Ringdal, F. (2006). The detection of low magnitude seismic events using
460 array-based waveform correlation. *Geophysical Journal International*, 165(1):149–166.
- 461 Goebel, T., Becker, T., Schorlemmer, D., Stanchits, S., Sammis, C., Rybacki, E., and
462 Dresen, G. (2012). Identifying fault heterogeneity through mapping spatial anomalies in
463 acoustic emission statistics. *Journal of Geophysical Research: Solid Earth*, 117(B3).
- 464 Hosseini, K. and Sigloch, K. (2017). Obspydmt: a python toolbox for retrieving and pro-
465 cessing large seismological data sets. *Solid Earth*, (5):1047–1070.
- 466 Hunstad, I. and England, P. (1999). An upper bound on the rate of strain in the central
467 apennines, italy, from triangulation measurements between 1869 and 1963. *Earth and*
468 *Planetary Science Letters*, 169(3-4):261–267.
- 469 Jones, L. M. and Molnar, P. (1979). Some characteristics of foreshocks and their pos-
470 sible relationship to earthquake prediction and premonitory slip on faults. *Journal of*
471 *Geophysical Research: Solid Earth*, 84(B7):3596–3608.
- 472 Jones, L. M. (1985). Foreshocks and time-dependent earthquake hazard assessment in
473 southern california. *Bulletin of the Seismological Society of America*, 75(6):1669–1679.
- 474 Kagan, Y. and Jackson, D. D. (1991). Long-term earthquake clustering. *Geophysical Journal*
475 *International*, 104(1):117–133.

- 476 Kagan, Y. and Knopoff, L. (1978). Statistical study of the occurrence of shallow earth-
477 quakes. *Geophysical Journal International*, 55(1):67–86.
- 478 Kato, A., Obara, K., Igarashi, T., Tsuruoka, H., Nakagawa, S., and Hirata, N. (2012).
479 Propagation of slow slip leading up to the 2011 mw 9.0 tohoku-oki earthquake. *Science*,
480 335(6069):705–708.
- 481 Liu, Y. and Rice, J. R. (2005). Aseismic slip transients emerge spontaneously in three-
482 dimensional rate and state modeling of subduction earthquake sequences. *Journal of*
483 *Geophysical Research: Solid Earth*, 110(B8).
- 484 Malin, P. E., Bohnhoff, M., Blümle, F., Dresen, G., Martínez-Garzón, P., Nurlu, M., Ceken,
485 U., Kadirioglu, F. T., Kartal, R. F., Kilic, T., et al. (2018). Microearthquakes preceding
486 a m4. 2 earthquake offshore istanbul. *Scientific reports*, 8(1):1–11.
- 487 Marone, C. (1998). The effect of loading rate on static friction and the rate of fault healing
488 during the earthquake cycle. *Nature*, 391(6662):69–72.
- 489 McLaskey, G. C. (2019). Earthquake initiation from laboratory observations and implica-
490 tions for foreshocks. *Journal of Geophysical Research: Solid Earth*.
- 491 McMahon, N. D., Aster, R. C., Yeck, W. L., McNamara, D. E., and Benz, H. M. (2017).
492 Spatiotemporal evolution of the 2011 prague, oklahoma, aftershock sequence revealed
493 using subspace detection and relocation. *Geophysical Research Letters*, 44(14):7149–7158.
- 494 McMahon, N. D., Yeck, W. L., Stickney, M. C., Aster, R. C., Martens, H. R., and Benz,
495 H. M. (2019). Spatiotemporal analysis of the foreshock–mainshock–aftershock sequence
496 of the 6 july 2017 m w 5.8 lincoln, montana, earthquake. *Seismological Research Letters*,
497 90(1):131–139.
- 498 Mignan, A. (2014). The debate on the prognostic value of earthquake foreshocks: A meta-
499 analysis. *Scientific reports*, 4:4099.

- 500 Mogi, K. (1963). Some discussions on aftershocks, foreshocks and earthquake swarms:
501 the fracture of a semi-infinite body caused by an inner stress origin and its relation to
502 the earthquake phenomena (third paper). *Bulletin of the Earthquake Research Institute,*
503 *University of Tokyo*, 41(3):615–658.
- 504 Molchanov, O., Hayakawa, M., Oudoh, T., and Kawai, E. (1998). Precursory effects in the
505 subionospheric vlf signals for the kobe earthquake. *Physics of the Earth and Planetary*
506 *Interiors*, 105(3-4):239–248.
- 507 Papazachos, B. (1975). Foreshocks and earthquake prediction. *Tectonophysics*, 28(4):213–
508 226.
- 509 Pedregosa, F., Varoquaux, G., Gramfort, A., Michel, V., Thirion, B., Grisel, O., Blondel,
510 M., Prettenhofer, P., Weiss, R., Dubourg, V., Vanderplas, J., Passos, A., Cournapeau,
511 D., Brucher, M., Perrot, M., and Duchesnay, E. (2011). Scikit-learn: Machine learning
512 in Python. *Journal of Machine Learning Research*, 12:2825–2830.
- 513 Reasenberg, P. A. (1999). Foreshock occurrence before large earthquakes. *Journal of*
514 *Geophysical Research: Solid Earth*, 104(B3):4755–4768.
- 515 Renard, F., McBeck, J., Kandula, N., Cordonnier, B., Meakin, P., and Ben-Zion, Y. (2019).
516 Volumetric and shear processes in crystalline rock approaching faulting. *Proceedings of*
517 *the National Academy of Sciences*, 116(33):16234–16239.
- 518 Rikitake, T. (1975). Earthquake precursors. *Bulletin of the Seismological Society of Amer-*
519 *ica*, 65(5):1133–1162.
- 520 Roberts, G. P. and Michetti, A. M. (2004). Spatial and temporal variations in growth rates
521 along active normal fault systems: an example from the lazio–abruzzo apennines, central
522 italy. *Journal of Structural Geology*, 26(2):339–376.

- 523 Rubin, A. M. and Ampuero, J.-P. (2005). Earthquake nucleation on (aging) rate and state
524 faults. *Journal of Geophysical Research: Solid Earth*, 110(B11).
- 525 Ruiz, S., Aden-Antoniow, F., Baez, J., Otarola, C., Potin, B., del Campo, F., Poli, P.,
526 Flores, C., Satriano, C., Leyton, F., et al. (2017). Nucleation phase and dynamic inversion
527 of the mw 6.9 valparaíso 2017 earthquake in central chile. *Geophysical Research Letters*,
528 44(20):10–290.
- 529 Ruiz, S., Metois, M., Fuenzalida, A., Ruiz, J., Leyton, F., Grandin, R., Vigny, C.,
530 Madariaga, R., and Campos, J. (2014a). Intense foreshocks and a slow slip event preceded
531 the 2014 iquique mw 8.1 earthquake. *Science*, 345(6201):1165–1169.
- 532 Ruiz, S., Metois, M., Fuenzalida, A., Ruiz, J., Leyton, F., Grandin, R., Vigny, C.,
533 Madariaga, R., and Campos, J. (2014b). Intense foreshocks and a slow slip event preceded
534 the 2014 iquique mw 8.1 earthquake. *Science*, 345(6201):1165–1169.
- 535 Savage, H. M., Keranen, K. M., P. Schaff, D., and Dieck, C. (2017). Possible precursory
536 signals in damage zone foreshocks. *Geophysical Research Letters*, 44(11):5411–5417.
- 537 Schoenball, M. and Ellsworth, W. L. (2017). A systematic assessment of the spatiotemporal
538 evolution of fault activation through induced seismicity in oklahoma and southern kansas.
539 *Journal of Geophysical Research: Solid Earth*, 122(12):10–189.
- 540 Schurr, B., Asch, G., Hainzl, S., Bedford, J., Hoechner, A., Palo, M., Wang, R., Moreno,
541 M., Bartsch, M., Zhang, Y., et al. (2014). Gradual unlocking of plate boundary controlled
542 initiation of the 2014 iquique earthquake. *Nature*, 512(7514):299–302.
- 543 Shelly, D. R., Beroza, G. C., and Ide, S. (2007). Complex evolution of transient slip de-
544 rived from precise tremor locations in western shikoku, japan. *Geochemistry, Geophysics,
545 Geosystems*, 8(10).

- 546 Shelly, D. R. and Hardebeck, J. L. (2019). Illuminating faulting complexity of the 2017
547 yellowstone maple creek earthquake swarm. *Geophysical Research Letters*, 46(5):2544–
548 2552.
- 549 Shen, Z.-K., Jackson, D. D., Feng, Y., Cline, M., Kim, M., Fang, P., and Bock, Y. (1994).
550 Postseismic deformation following the landers earthquake, california, 28 june 1992. *Bulletin
551 of the Seismological Society of America*, 84(3):780–791.
- 552 Singh, R. P., Mehdi, W., Gautam, R., Senthil Kumar, J., Zlotnicki, J., and Kafatos, M.
553 (2010). Precursory signals using satellite and ground data associated with the wenchuan
554 earthquake of 12 may 2008. *International Journal of Remote Sensing*, 31(13):3341–3354.
- 555 Stein, R. S. and Lisowski, M. (1983). The 1979 homestead valley earthquake sequence,
556 califonia: Control of aftershocks and postseismic deformation. *Journal of Geophysical
557 Research: Solid Earth*, 88(B8):6477–6490.
- 558 Tape, C., Holtkamp, S., Silwal, V., Hawthorne, J., Kaneko, Y., Ampuero, J. P., Ji, C.,
559 Ruppert, N., Smith, K., and West, M. E. (2018). Earthquake nucleation and fault slip
560 complexity in the lower crust of central alaska. *Nature Geoscience*, 11(7):536–541.
- 561 Toda, S., Stein, R. S., Sevilgen, V., and Lin, J. (2011). Coulomb 3.3 graphic-rich defor-
562 mation and stress-change software for earthquake, tectonic, and volcano research and
563 teachinguser guide. *US Geological Survey open-file report*, 1060(2011):63.
- 564 Uchida, N. (2019). Detection of repeating earthquakes and their application in character-
565 izing slow fault slip. *Progress in Earth and Planetary Science*, 6(1):40.
- 566 Uchida, N. and Bürgmann, R. (2019). Repeating earthquakes. *Annual Review of Earth and
567 Planetary Sciences*, 47:305–332.
- 568 Tramutoli, V., Corrado, R., Filizzola, C., Genzano, N., Lisi, M., and Pergola, N. (2015).
569 From visual comparison to robust satellite techniques: 30 years of thermal infrared satel-

- lite data analyses for the study of earthquake preparation phases. *Bollettino di Geofisica Teorica ed Applicata*, 56(2).
- Trugman, D. T., Ross, Z. E., and Johnson, P. A. (2020). Imaging stress and faulting complexity through earthquake waveform similarity. *Geophysical Research Letters*, 47(1):e2019GL085888.
- Virk, H. and Walia, V. (2001). Helium/radon precursory signals of chamoli earthquake, india. *Radiation measurements*, 34(1-6):379–384.
- Waldhauser, F. (2001). hypodda program to compute double-difference hypocenter locations (hypodd version 1.0-03/2001). *US Geol. Surv. Open File Rep.*, 01, 113.
- Ward Jr, J. H. (1963). Hierarchical grouping to optimize an objective function. *Journal of the American statistical association*, 58(301):236–244.
- Wedmore, L., Walker, J. F., Roberts, G. P., Sammonds, P., McCaffrey, K., and Cowie, P. (2017). A 667 year record of coseismic and interseismic coulomb stress changes in central italy reveals the role of fault interaction in controlling irregular earthquake recurrence intervals. *Journal of Geophysical Research: Solid Earth*, 122(7):5691–5711.
- Wehling-Benatelli, S., Becker, D., Bischoff, M., Friederich, W., and Meier, T. (2013). Indications for different types of brittle failure due to active coal mining using waveform similarities of induced seismic events. *Solid Earth*, 4(2).
- Wessel, P. and Smith, W. H. (1998). New, improved version of generic mapping tools released. *Eos, Transactions American Geophysical Union*, 79(47):579–579.
- Westaway, R. (1992). Seismic moment summation for historical earthquakes in italy: tectonic implications. *Journal of Geophysical Research: Solid Earth*, 97(B11):15437–15464.

- 592 Yoon, C. E., Yoshimitsu, N., Ellsworth, W. L., and Beroza, G. C. (2019). Foreshocks and
593 mainshock nucleation of the 1999 m w 7.1 hector mine, california, earthquake. *Journal*
594 *of Geophysical Research: Solid Earth*, 124(2):1569–1582.
- 595 Zang, A., Christian Wagner, F., Stanchits, S., Dresen, G., Andresen, R., and Haidekker,
596 M. A. (1998). Source analysis of acoustic emissions in aue granite cores under symmetric
597 and asymmetric compressive loads. *Geophysical Journal International*, 135(3):1113–1130.

598 **Figure Captions**

Figure 1. Regional map of the study area. The yellow square inside the small map inset on the left corresponds to the central region of Italy represented in the larger topographic map. The small map inset on the right represents magnification of the black dashed area around the epicentral location (red star). The color code used in the map view on the right represents the estimated depth of the foreshock and aftershock activity (estimated in this study: 714 events). The yellow circle represents Balsorano city, and the white triangles represent the stations used in this study. The dashed lines in the right inset map represent the directions A-A' (along strike) and B-B' (normal to the strike) illustrated in the cross sections of Figure 5. The solid red line represents the superficial scarp of the Liri fault (scarp taken from [Wedmore et al. \(2017\)](#)).

Figure 2. (a) Spectrogram on VVLD.HHZ. The white line is the median of the energy in the frequency band between 5 Hz and 20 Hz calculated within a 1-h sliding window. Notice the diurnal energy variation. (b) Blue, cumulative events for the same time period of the experiment; orange, recurrence time for the newly detected events. (c) Estimated magnitudes for the newly detected events. A gap in the continuous data at this receiver location is seen for the night of November 8 to 9, 2019. In all pannels, day and night periods are represented by shaded (18:00 to 6:00) and unshaded (6:00 to 18:00) regions.

Figure 3. Illustration of the waveform-based hierarchical clustering output. (a) Pairwise correlation coefficients between the waveforms for the vertical component of station VVLD (Fig. 1) of the 714 detected events. This matrix is used to perform the hierarchical clustering. (b) Cumulative events combined with the results from the hierarchical clustering, according to the color code in the legend. (c) Characteristic normalized waveforms (vertical

component) of the five different clusters revealed in the earthquake sequence. These traces are obtained after stacking all of the individually normalized waveforms belonging to each cluster.

Figure 4. Spatio-temporal evolution of the earthquake sequences with respect to the mainshock origin time and hypocenter. Left column: Temporal density (number of events per hour). The coefficients of variation (COV) from the recurrence times are indicated for each cluster. Black dashed line, mainshock hypocenter and origin time. Center column: Distance in time and space from each event of the sequence with respect to the mainshock location and origin time. Black The dashed line, mainshock hypocenter grey line on the left and center column represents the mainshock origin time. Right column: Spatial density (concentration of events per 0.1 km). Solid Dashed black line, where 90% of the seismic activity is concentrated. (a)-(e) Each of the five clusters. clusters progressively ordered. The same color code from Figure 3 is used.

Figure 5. Map view (left column), and cross-sections along the strike (middle column) and normal-strike (right column) directions for each of the five clusters identified in the sequence (as indicated). All of the locations are relative to the mainshock hypocenter (41.7746°N 13.6066°E ; 13.94 km depth, black star). In all of the panels, the same color code is used as in Figures 3 and 4 to represent each different cluster. The solid black line represents a fault plane of 1 km^2 with the geometry of the second nodal plane (Supplementary Materials Table S1). The dashed blue line represents the assumed auxiliary nodal plane. The directions A-A' (along strike) and B-B' (normal to the strike) are the same as in Figure 1. 1. Each cluster is represented by a correponding label a) Cluster 1 , b) Cluster 2, c) Cluster 3, d) Cluster 4 and e) Cluster 5. In each panel, the black circles represent the location of the templates belonging to each cluster.

599 Figures

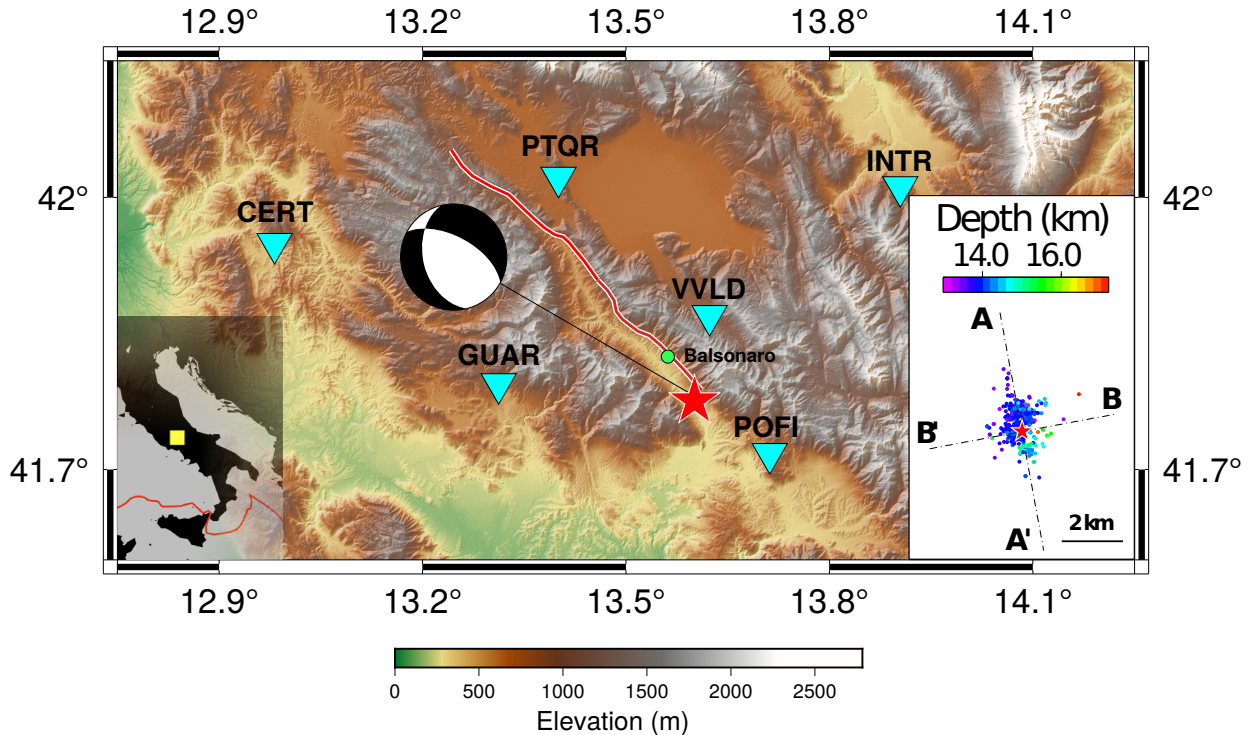


Figure 1: Regional map of the study area. The yellow square inside the small map inset on the left corresponds to the central region of Italy represented in the larger topographic map. The small map inset on the right represents magnification of the black dashed area around the epicentral location (red star). The color code used in the map view on the right represents the estimated depth of the foreshock and aftershock activity (estimated in this study: 714 events). The yellow circle represents Balsorano city, and the white triangles represent the stations used in this study. The dashed lines in the right inset map represent the directions A-A' (along strike) and B-B' (normal to the strike) illustrated in the cross sections of Figure 5. 5. The solid red line represents the superficial scarp of the Liri fault (scarp taken from [Wedmore et al. \(2017\)](#)).

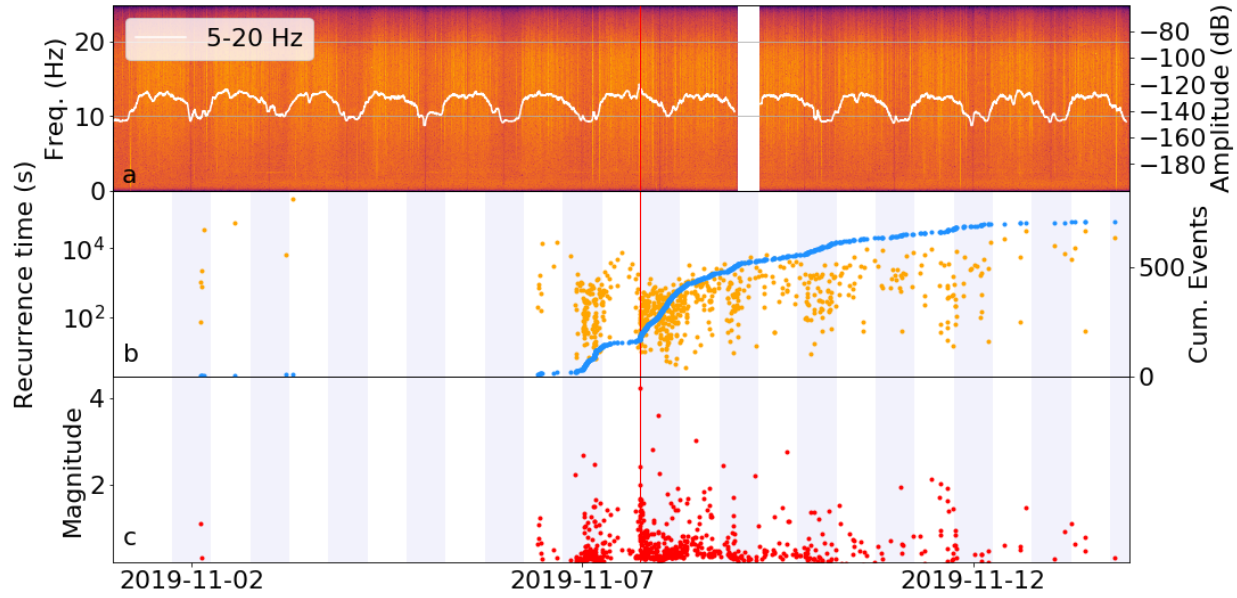


Figure 2: (a) Spectrogram on VVLD.HHZ. The white line is the median of the energy in the frequency band between 5 Hz and 20 Hz calculated within a 1-h sliding window. Notice the diurnal energy variation. (b) Blue, cumulative events for the same time period of the experiment; orange, recurrence time for the newly detected events. (c) Estimated magnitudes for the newly detected events. A gap in the continuous data at this receiver location is seen for the night of November 8 to 9, 2019. In all pannels, day and night periods are represented by shaded (18:00 to 6:00) and unshaded (6:00 to 18:00) regions.

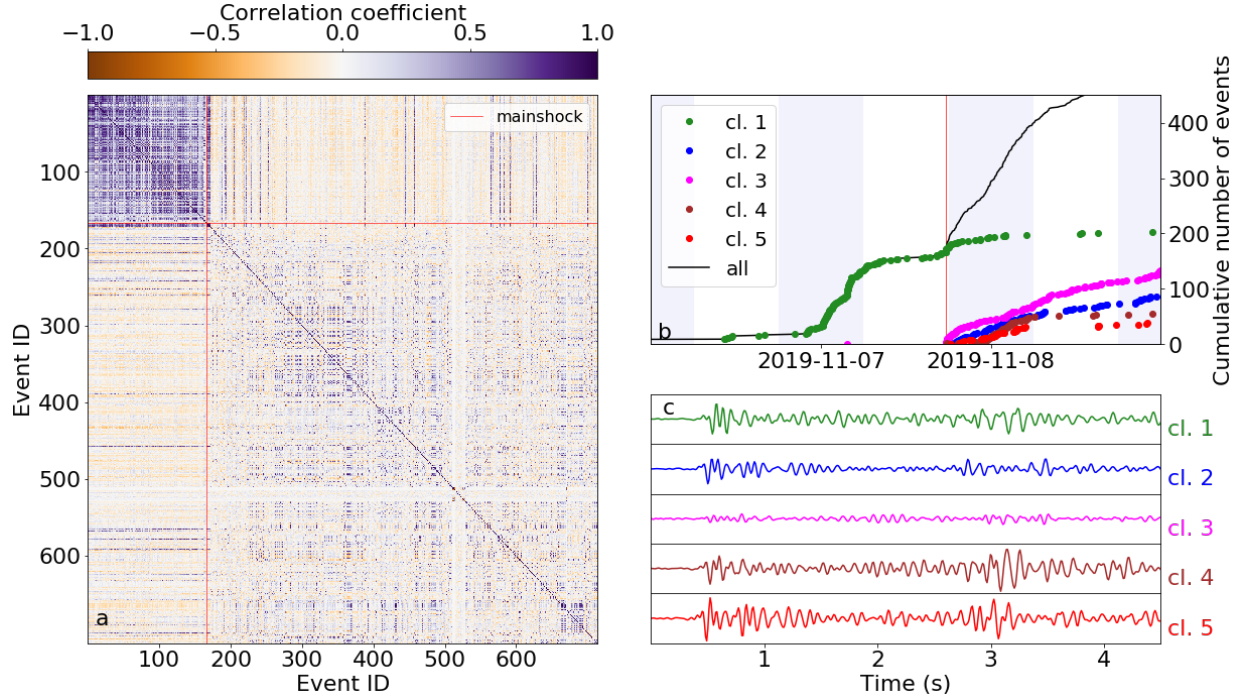


Figure 3: Illustration of the waveform-based hierarchical clustering output. (a) Pairwise correlation coefficients between the waveforms for the vertical component of station VVLD (Fig. 1) of the 714 detected events. This matrix is used to perform the hierarchical clustering. (b) Cumulative events combined with the results from the hierarchical clustering, according to the color code in the legend. (c) Characteristic normalized waveforms (vertical component) of the five different clusters revealed in the earthquake sequence. These traces are obtained after stacking all of the individually normalized waveforms belonging to each cluster.

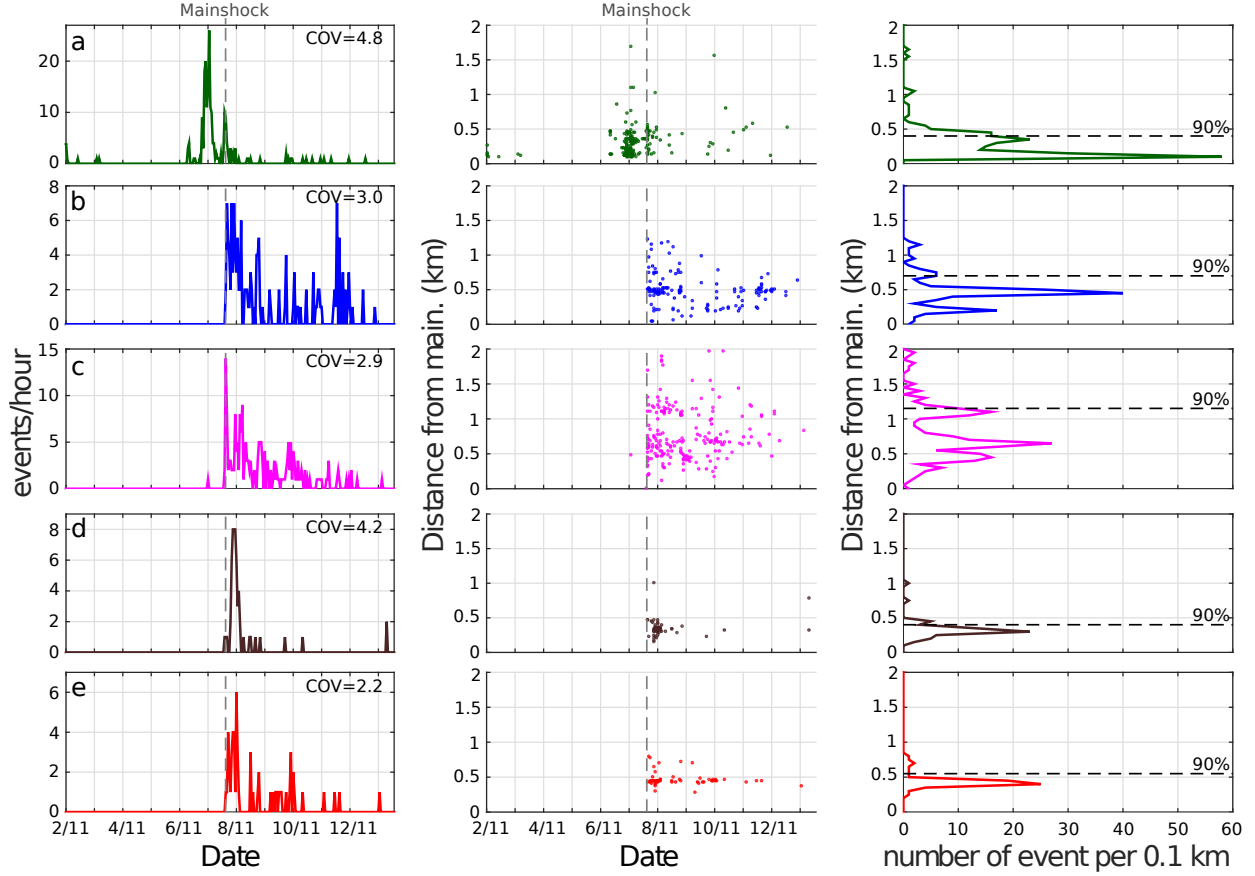


Figure 4: Spatio-temporal evolution of the earthquake sequences with respect to the mainshock origin time and hypocenter. Left column: Temporal density (number of events per hour). The coefficients of variation (COV) from the recurrence times are indicated for each cluster. Black dashed line, mainshock hypocenter and origin time. Center column: Distance in time and space from each event of the sequence with respect to the mainshock location and origin time. Black The dashed line, mainshock hypocenter grey line on the left and center column represents the mainshock origin time. Right column: Spatial density (concentration of events per 0.1 km). Solid Dashed black line, where 90% of the seismic activity is concentrated. (a)-(e) Each of the five clusters. clusters progressively ordered. The same color code from Figure 3 is used.

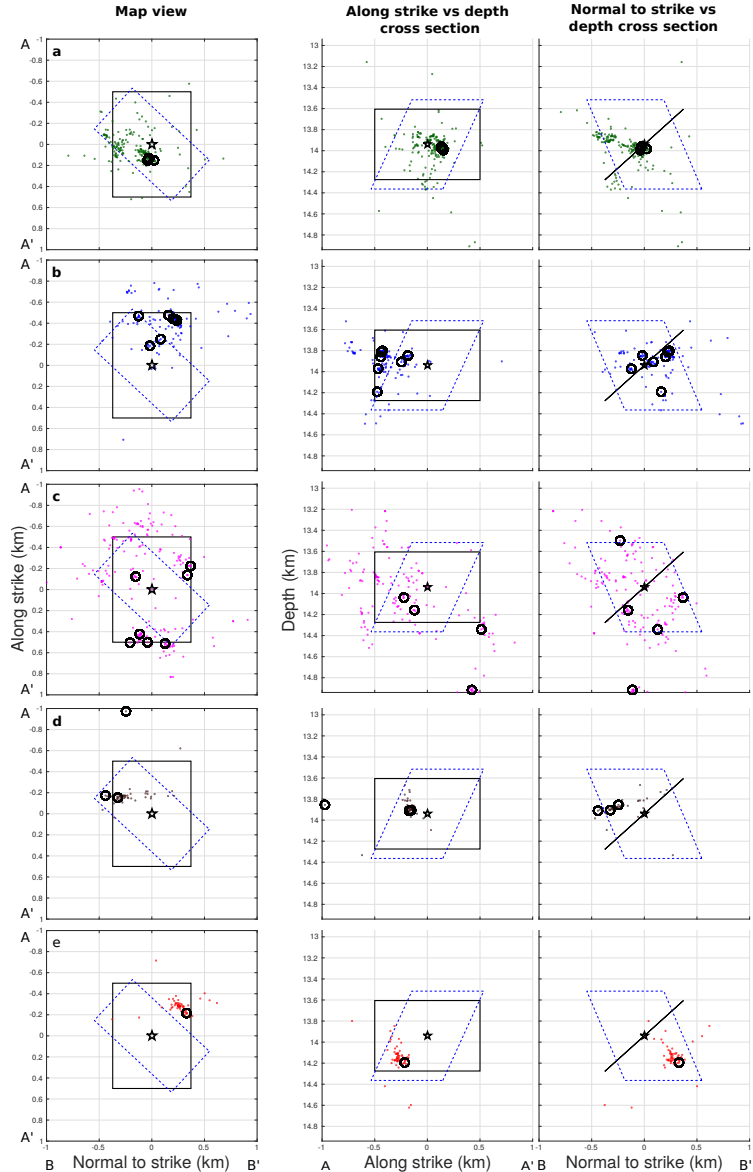


Figure 5: Map view (left column), and cross-sections along the strike (middle column) and normal-strike (right column) directions for each of the five clusters identified in the sequence (as indicated). All of the locations are relative to the mainshock hypocenter (41.7746°N 13.6066°E ; 13.94 km depth, black star). In all of the panels, the same color code is used as in Figures 3 and 4 to represent each different cluster. The solid black line represents a fault plane of 1 km^2 with the geometry of the second nodal plane (Supplementary Materials Table S1). The dashed blue line represents the assumed auxiliary nodal plane. The directions A-A' (along strike) and B-B' (normal to the strike) are the same as in Figure 1.

1. Each cluster is represented by a correponding label a) Cluster 1 , b) Cluster 2, c) Cluster 3, d) Cluster 33
 e) Cluster 5. In each panel, the black circles represent the location of the templates belonging to each cluster.